Physics of Plasmas

RESEARCH ARTICLE | NOVEMBER 02 2023

Self-consistent coupling of JOREK and CARIDDI: On the electromagnetic interaction of 3D tokamak plasmas with 3D volumetric conductors

N. Isernia ; N. Schwarz ; F. J. Artola ; S. Ventre ; M. Hoelzl ; G. Rubinacci ; F. Villone ;
JOREK Team

Phys. Plasmas 30, 113901 (2023)
https://doi.org/10.1063/5.0167271

Physics of Plasmas ARTICLE pubs.aip.org/aip/pop

Self-consistent coupling of JOREK and CARIDDI: On the electromagnetic interaction of 3D tokamak plasmas with 3D volumetric conductors

Cite as: Phys. Plasmas **30**, 113901 (2023); doi: 10.1063/5.0167271
Submitted: 11 July 2023 · Accepted: 4 October 2023 ·
Published Online: 2 November 2023

View Online Export Citation CrossMark

N. Isernia,[1,a)] N. Schwarz,[2] F. J. Artola,[3] S. Ventre,[4] M. Hoelzl,[2] G. Rubinacci,[5] F. Villone,[1] and JOREK Team[b)]

AFFILIATIONS

[1]Dipartimento di Ingegneria Elettrica e delle Tecnologie dell'Informazione, Università degli Studi di Napoli Federico II, Via Claudio 21, 80125 Napoli, Italy
[2]Max Planck Institute for Plasma Physics, Boltzmannstrasse 2, 85748 Garching, Germany
[3]ITER Organization, 13067 St. Paul Lez Durance Cedex, France
[4]Dipartimento di Ingegneria Elettrica e dell'Informazione, Università di Cassino e del Lazio Meridionale, Via Gaetano di Biasio 43, 03043 Cassino, Italy
[5]CREATE Consortium, Università degli Studi di Napoli Federico II, Via Claudio 21, 80125 Napoli, Italy

[a)]**Author to whom correspondence should be addressed:** nicola.isernia@unina.it
[b)]See the author list of Hoelzl *et al.*, "The JOREK non-linear extended MHD code and applications to large-scale instabilities and their control in magnetically confined fusion plasmas," Nucl. Fusion **61**, 065001 (2021).

ABSTRACT

The self-consistent electromagnetic integration of tokamak plasma magnetohydrodynamic (MHD) models with external conductors is considered in this manuscript. We integrate the extended MHD code JOREK and the eddy current code CARIDDI, via a scheme based on the virtual casing principle enabling two-way coupled fully implicit simulations. The robustness of this new integrated tool is validated against JOREK-STARWALL and CarMa0NL simulations for vertical displacement events in a simplified ASDEX Upgrade-like geometry and for $n = 1$ tearing modes in a circular high-aspect-ratio tokamak. The impact of 3D wall structures on the plasma evolution is highlighted introducing ports at different locations of a simplified axisymmetric wall and characterizing its effect on the plasma evolution. In addition to realistically capturing the 3D interactions between plasma and wall structures, the coupled codes will allow in the future 1:1 comparisons to experiments using virtual magnetic diagnostics that capture screening effects accurately.

I. INTRODUCTION: THE PLASMA–WALL ELECTROMAGNETIC INTERACTION

Modeling the electro magnetic interaction between tokamak plasmas and surrounding conductive structures is essential for understanding the macroscopic plasma dynamics, the arising forces onto these structures, and thus for advancing fusion device design. Plasma motion and current profile variations induce eddy currents in the surrounding passive structures that in turn impact the evolution of the plasma. This feedback mechanism is far from negligible: the inertia to the motion offered by the reaction magnetic field from passive conductors can be concurrent or even overwhelm the plasma mechanical inertia itself in certain conditions. This is the case also for several unstable magnetohydrodynamic (MHD) modes. The most widely known example is the axisymmetric instability respect to vertical displacements in plasmas with elongated cross section.[2–5] For this type of MHD instability, often simplified mass-less models are sufficient to capture the phenomenon.[6–8] Also, external kink modes are affected by the interaction with surrounding conductors,[9,10] allowing to operate tokamak experiments above the no-wall beta limit.[11,12]

The literature has demonstrated that the 3D features of the conductors can significantly impact the growth rate estimations of both axisymmetric[13,14] and non-axisymmetric[15,16] MHD instabilities. Moreover, the skin depth of the magnetic perturbation can be comparable to standard wall widths for some MHD modes.[17] Hence, the thin wall assumption, often adopted in the literature, is not always robust. In addition to this, the integrated modeling of plasma dynamics in the presence of external conductors is limited either to a simplified representation of conductive structures or to a simplified plasma model.

The non-linear MHD code M3D[18] was coupled exclusively to an axisymmetric thin model of passive structures.[19] Although in a different stream, also the visco-resistive MHD code NIMROD[20] was coupled exclusively to an axisymmetric thin model of passive conductors.[21,22] In M3D-C[1],[23,24] the conductors and a portion of the vacuum domain were included within the standard computational domain[25] limiting details that can be captured in conducting structures. JOREK-STARWALL (JS)[26,27] is the only non-linear extended MHD code, which includes the possibility of describing 3D conductive structures self-consistently, although these are limited to be thin. Integrated MHD linear models like CASTOR3D,[28,29] VALEN,[30] and MARS-F[31,32] describe exclusively thin conductors. The latter can model 3D active coils but is limited to axisymmetric conductors for the passive structures. These limitations, besides conceptual, are also practical: the reduction of complex volumetric geometries to thin meshes can be a difficult task in practice.

On the other hand, models capable of a realistic, volumetric description of conductive structures have so far adopted simplifying assumptions regarding the plasma model. Based on the mass-less assumption, both non-linear axisymmetric models[8,33] as well as linearized 3D models[34] were established. The latter was recently extended to account for the plasma inertia,[35] representing the first linear dynamic MHD model interacting with fully 3D volumetric conductors. Reference 8 contains an overview of the modeling landscape.

To overcome the limitations described above, we integrate the 3D non-linear extended MHD model JOREK[1,36,37] with the fully 3D volumetric model of passive conductors CARIDDI[38–40] in this manuscript. The approach adopted here is based on the virtual casing principle, like it was already adopted for JOREK-STARWALL.[26,27]

We review the possible coupling strategies, providing in particular also details for the indirect scheme adopted here in Sec. II. In Sec. III, we focus on the equivalent surface current at the MHD computational boundary, which describes plasma magnetic fields in the outer domain, performing a sensitivity scan in the relevant numerical parameters. Successively, the coupled JOREK-CARIDDI (JC) codes are first validated against JOREK-STARWALL and CarMa0NL axi-symmetric vertical displacement event (VDE) simulations in Sec. IV. In this three-way benchmark, we also stress the different physics included in JOREK and CarMa0NL for describing the plasma, assessing the validity of the mass-less hypothesis for the considered ASDEX Upgrade (AUG) like example. A simple circular high-aspect-ratio tokamak is considered in Sec. V, to benchmark the correct description of a tearing mode instability, validating this way the coupling scheme also for higher-order toroidal harmonics. Finally in Sec. VI, we explore how the 3D wall structures affect the coupling of otherwise linearly independent MHD modes, comparing several setups with different port openings in an otherwise axisymmetric tokamak wall both between JOREK-CARIDDI and JOREK-STARWALL. The satisfactory quantitative agreement of our benchmarks proves the efficacy of the integrated JOREK-CARIDDI tool for the non-linear analysis of MHD instabilities coupled with currents in external 3D volumetric conductors rendering advanced research applications possible in the future that could previously not be addressed.

II. MATHEMATICAL FORMULATION

For clarity, let us define as "interior" or "inner" domain the MHD computational domain V_{in}, described within the JOREK framework here (discretized by finite elements). Consistently by "exterior" or "outer" domain, we point out all the physical space outside of the MHD computational boundary $V_{ext} = \mathbb{E}_3 \backslash V_{in}$, where $\mathbb{E}_3$ is the overall three-dimensional Euclidean space. A schematic picture is provided in Fig. 1. The correct solution of the MHD equations in the JOREK formulation requires to assign a number of boundary conditions at the MHD computational boundary $+\partial V_{in}$. Among these, the tangential component of the magnetic field $\mathbf{B} \times \mathbf{n}$ needs to be assigned at each time instant of the simulation. The determination of such a boundary condition requires the solution of the Magneto-Quasi-Static (MQS) problem in the exterior domain, where active and passive currents are allowed to flow. The static counterpart for this problem is the solution of the outer magneto-static problem, necessary to provide boundary conditions for the solution of free-boundary MHD equilibria. The standard in this context is to reduce the outer magneto-static problem to a boundary integral equation, exploiting properly Green function theorems.[41,42] Several strategies are available in the context of fusion plasmas, where the toroidal topology of the domain plays an important role, at least for the purely axisymmetric problem,[6,43,44] a synthetic review is found in Ref. 45. The solution of the outer MQS problem proposed here can be classified as an *indirect* or *Bielak–MacCamy* method, and is based on the *Virtual Casing Principle.*[46] In Subsection II A, we introduce the electromagnetic boundary conditions required by the reduced MHD JOREK models. The model adopted for external conductors is shortly reviewed in Subsection II B. In Subsection II C, we translate the vector potential at the MHD computational boundary into an equivalent surface current, which correctly describes fields and potentials due to the plasma in the exterior domain. The resulting formulation, similar to the JOREK-STARWALL[26] one, is resumed in Subsection II D. Also, the parallel I/O and the distribution among processes of the coupling matrices in JOREK[47] are taken over from JOREK-STARWALL to JOREK-CARIDDI.

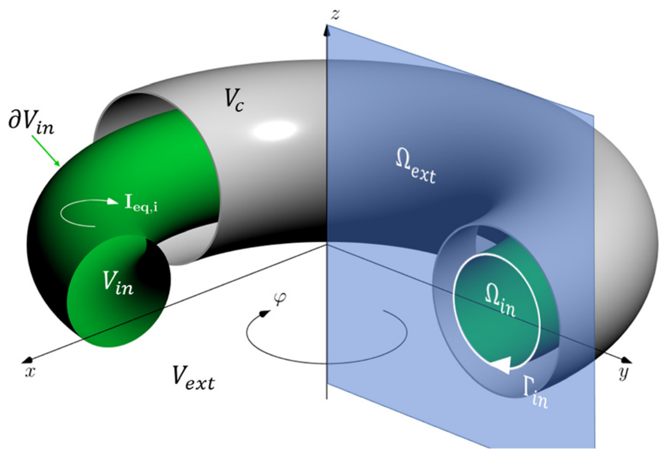

FIG. 1. Definition of interior domain V_{in}, exterior domain $V_{ext,}$ and coupling surface $+\partial V_{in}$.

A. JOREK boundary conditions

JOREK is a numerical code for the solution of a family of different extended MHD models with the possible inclusion of neutrals, impurities, runaway electrons, and an extension to include kinetic models.[1] A common feature for all the physics models is the use of the magnetic vector potential $\mathbf{A}$ as one of the primary unknown variables. Within this family, the most popular models are based on the reduced MHD approximation, which allows to neglect fast magneto-sonic waves from the analysis and reduce drastically the computational costs.[36] The reduced version of the MHD equations is obtained by the ansatz

$$\mathbf{A} = \psi \nabla \varphi, \tag{1}$$

where ψ is defined as poloidal flux, and φ is the toroidal angle. The full MHD model integrates all components of the vector potential using the Weyl gauge in JOREK,[48] setting to zero the electric scalar potential (i.e., $\phi = 0$). The limit of the reduced MHD approach is discussed in 1 and 48.

In this manuscript, we address the coupling of reduced MHD JOREK models with the external conductive structures leaving full MHD coupling to future work. In this case, the boundary condition to assign is related solely to the normal derivative of the poloidal flux,[27] i.e., $(1/r)\partial\psi/\partial n$. In particular, the projection along the φ direction of Ampére's law $\nabla \times \nabla \times \mathbf{A} = \mu_0 \mathbf{j}$ gets the form

$$-\mu_0 r j_\varphi = r\left[\frac{\partial}{\partial r}\left(\frac{\partial_r \psi}{r}\right) + \frac{\partial}{\partial z}\left(\frac{\partial_z \psi}{r}\right)\right] = \Delta^* \psi. \tag{2}$$

The above expression defines the operator Δ^*. At this stage, $j = -\mu_0 r j_\varphi$ is introduced as a support variable for the MHD problem and Eq. (2) is enforced in weak form against test functions λ. Integrating by parts, we get easily to the equation

$$\int_0^{2\pi}\int_{\Omega_{in}} \frac{\lambda}{r}\cdot j \mathrm{d}S\mathrm{d}\varphi = \int_0^{2\pi}\int_{\Gamma_{in}} \lambda \frac{1}{r}\frac{\partial \psi}{\partial n}\mathrm{d}\ell \mathrm{d}\varphi - \int_0^{2\pi}\int_{\Omega_{in}} \frac{1}{r^2}\nabla_\perp \psi \cdot \nabla_\perp \lambda \mathrm{d}S\mathrm{d}\varphi. \tag{3}$$

The electromagnetic boundary condition to assign is related to the surface term above, which is related solely to the normal derivative of the poloidal flux, i.e., $(1/r)\partial\psi\partial n$. This is only a portion of the poloidal component of the magnetic field tangent to the boundary, which excludes spatial derivatives of A_r and A_z. On the other hand, in *full* MHD models, the tangential magnetic field to the boundary has to be provided in its integrity; i.e., we have to provide both B_θ and B_φ at the boundary as functions of ψ and A_θ. Here, we have indicated by the subscript θ the poloidal component of vector fields tangent to the computational boundary of JOREK. Also, future stellarator applications will require two non-zero components of $\mathbf{B} \times \mathbf{n}$ as boundary condition.

The test functions λ introduced in Eq. (3) are clearly JOREK basis functions, so to configure a Galerkin method. Scalar fields are represented in JOREK using a spectral decomposition along the toroidal angle, i.e., via a Fourier series of the angle φ, and a discretization via finite elements in the poloidal plane. In particular, an iso-parametric G^1 finite element space is constructed in the poloidal plane via Bezier patches.[37]

B. CARIDDI model of conductors

The MQS problem in the outer domain V_{ext} is solved via an integral formulation, which allows to discretize exclusively the region of conductors V_c, rather than the whole exterior domain. In particular, the electric field can be expressed in terms of the electromagnetic potentials

$$\mathbf{E} = -\frac{\partial \mathbf{A}}{\partial t} - \nabla \phi, \tag{4}$$

so that Faraday's law is automatically satisfied. Furthermore, in the Coulomb gauge, we can set up the Biot–Savart law

$$\mathbf{A} = \frac{\mu_0}{4\pi}\int_{V_c} \frac{\mathbf{j}(\mathbf{x}')}{|\mathbf{x}-\mathbf{x}'|}\mathrm{d}V' + \mathbf{A_s}, \tag{5}$$

which guarantees Ampére's law to be satisfied. The term $\mathbf{A_s}$ above represent the magnetic vector potential produced by some known source, which in our case is the plasma contained in the inner domain, i.e., $\mathbf{A_s} = \mathbf{A_{in}}$. We shall see how to evaluate $\mathbf{A}_s$ in Sec. II C. Plugging (4) and (5) into the constitutive equation for the linear conductors, we get

$$\eta \mathbf{j} = -\frac{\mathrm{d}}{\mathrm{d}t}\left[\frac{\mu_0}{4\pi}\int_{V_c}\frac{\mathbf{j}(\mathbf{x}')}{|\mathbf{x}-\mathbf{x}'|}\mathrm{d}V'\right] - \frac{\partial \mathbf{A_s}}{\partial t} - \nabla \phi. \tag{6}$$

The approximation is introduced precisely at this stage, as we enforce (6) only in weak form via a Galerkin method. The electric current density is approximated via a finite set of basis functions $V = \{\mathbf{w_k} \in \mathbf{L_2}(V_c)\}$, which serves also as space of test functions to enforce (6). The resulting discrete system of ordinary differential equations is

$$\underline{\underline{R_w}}\,\underline{I} + \underline{\underline{L_w}}\frac{\mathrm{d}}{\mathrm{d}t}\underline{I} + \underline{V_s} + \underline{\underline{F}}\,\underline{\phi} = \underline{0}. \tag{7}$$

In the circuit equations above, we have defined the vector of induced voltages due to variations of assigned current sources

$$(V_s)_i = \frac{\mathrm{d}}{\mathrm{d}t}\int_{V_c} \mathbf{w_i}\cdot \mathbf{A_s}\mathrm{d}V, \tag{8}$$

and the vector of applied voltages to eventual electrodes $\underline{\phi}$. The matrices defined in (7) are the resistance, inductance, and electrode incidence matrix as follows:

$$(R_w)_{i,j} = \int_{V_c} \mathbf{w_i}\cdot \eta \cdot \mathbf{w_j}\mathrm{d}V, \tag{9}$$

$$(L_w)_{i,j} = \frac{\mu_0}{4\pi}\int_{V_c}\int_{V_c}\frac{\mathbf{w_i}(\mathbf{x})\cdot \mathbf{w_j}(\mathbf{x}')}{|\mathbf{x}-\mathbf{x}'|}\mathrm{d}V'\mathrm{d}V, \tag{10}$$

$$F_{i,j} = \int_{S_j} \mathbf{w_i}\cdot \hat{\mathbf{n}}\mathrm{d}S. \tag{11}$$

In Eq. (11), we indicated by S_j distinct equi-potential electrodes. The incidence matrix $\underline{F}$ allows us to feed the active conductors via a voltage supply. In the following, we will exclude the possibility of having electrodes at the boundary of the conducting domain facing the plasma. The plasma-facing electrodes will need to be considered anyway in case of shared currents between plasma and conductors (also defined as *halo currents*), and will be object of future work on the subject. The magnetic field produced by the currents in the outer domain is evaluated at a finite set of points $\mathbf{x_i}$ at the outer page to the JOREK boundary via a Biot–Savart integral and projected along the poloidal tangent direction

$$(B'_{\theta,w})_{i,j} = \mathbf{i}_\theta(\mathbf{x_i}) \cdot \int_{V_c} \frac{\mu_0}{4\pi} \mathbf{w_j}(\mathbf{x}') \times \nabla' \frac{1}{|\mathbf{x_i} - \mathbf{x}'|} \mathrm{d}V'. \quad (12)$$

The scalar fields, whose samples are given by the columns of $B'_{\theta,w}$, are then represented via Bezier basis functions by solving a minimization problem, and the resulting matrix is indicated by $B_{\theta,w}$. The basis function $\mathbf{w_j}$ in CARIDDI is divergence-free and easily associated to mesh edges.[38,39] In particular, in order to guarantee the electric current density to be a divergence-free vector field, an electric vector potential $\mathbf{T}$ is introduced such that $\mathbf{j} = \nabla \times \mathbf{T}$. The electric vector potential is then represented via *edge shape functions*, vector basis functions associated with the edges of the mesh. The electric current density is represented via the finite set of basis functions $V = \{\mathbf{w_k} = \nabla \times \mathbf{T_k}$ where $\mathbf{T_k} \in \mathbf{L_{2,curl}}(V_c) : \int_{e_i} \mathbf{T_k} \cdot \hat{\mathbf{t}} \mathrm{d}\ell = \delta_{i,k}\}$. The two-component gauge for $\mathbf{T}$ translates into a tree–cotree decomposition of the mesh in this framework: we can immediately set to zero all the basis vectors, which are associated with tree edges, reducing considerably the dimension of the space of basis functions necessary to the description of currents. Furthermore, this formulation allows to have tangential discontinuities of the electric current density across faces of the mesh, while preserving the normal component of the electric current density. This is a desirable feature in view of the many conductor–vacuum interfaces of typical tokamak conductors.

C. The virtual casing principle

Let us perform a virtual experiment, in absence of external currents, and assume that the interface between the inner domain and the outer domain is made by a perfect superconducting material. Any current raised within the inner domain will be perfectly shielded out by a surface current flowing along this boundary, so that in the outer domain, the magnetic field due to internal sources is canceled perfectly. We conclude that an equivalent surface current exists, at the boundary of the inner domain, which perfectly describes the interior currents' magnetic field in the outer domain. The outer magneto-static problem is completely specified also assigning the magnetic flux through any close curve laying on the same interface $+\partial V_{in}$. Finally, given the external currents, either an equivalent surface current to the plasma or the tangential component of the magnetic vector potential, contain equivalent information, hence a relation between the two exists. This is provided by the Biot–Savart law

$$\mathbf{A_{in}} = \frac{\mu_0}{4\pi} \int_{\partial V_{in}} \mathbf{k_{eq}}(\mathbf{x}') \cdot \frac{1}{|\mathbf{x} - \mathbf{x}'|} \mathrm{d}S' \quad \text{on } \partial V_{in}. \quad (13)$$

Here, we indicate by $\mathbf{A_{in}}$, the magnetic vector potential due to currents within the internal domain V_{in}, i.e., plasma currents. In general, the magnetic vector potential $\mathbf{A_{in}}$ could be assigned in any gauge; here, we impose Eq. (13) in weak form on a set of basis vectors, which is tangent to the interface and divergence-free therein, so that we immediately get rid of any gauge information

$$\int_{\partial V_{in}} \mathbf{w} \cdot \mathbf{A_{in}} \mathrm{d}\mathbf{S} = \int_{\partial V_{in}} \mathbf{w}(\mathbf{x}) \cdot \frac{\mu_0}{4\pi} \int_{\partial V_{in}} \mathbf{k_{eq}}(\mathbf{x}') \cdot \frac{1}{|\mathbf{x} - \mathbf{x}'|} \mathrm{d}S' \mathrm{d}S$$
$$\forall \mathbf{w} \in \mathbf{L_{2,div}}(\partial \mathbf{V_{in}}) : \mathrm{div}(\mathbf{w}) = 0. \quad (14)$$

Providing the possibility to approximate ∂V_{in} with a thin volumetric shell V_{eq}, we can use standard CARIDDI basis functions for current densities as test functions, $\{\mathbf{w_k} \in \mathbf{L_{2,div}}(V_{eq}) : \mathrm{div}(\mathbf{w_k}) = 0, \mathbf{w_k} \cdot \mathbf{n} = 0 \text{ on } \partial V_{eq}\}$. The intrinsic advantage is that representing the electric current density in the same space, we end up with the Galerkin formulation

$$\int_{V_{eq}} \mathbf{w_k} \cdot \mathbf{A_{in}} \mathrm{dV} = \sum_{j=1}^{n_{eq}} I_{eq,j} \int_{V_{eq}} \mathbf{w_k}(\mathbf{x}) \cdot \frac{\mu_0}{4\pi} \int_{V_{eq}} \mathbf{w_j}(\mathbf{x}') \cdot \frac{1}{|\mathbf{x} - \mathbf{x}'|} \mathrm{d}V' \mathrm{d}V. \quad (15)$$

Here, $\mathbf{w_k}$ represent the curl of a standard CARIDDI edge shape function, and we have an equation for each of the CARIDDI d.o.f. at the equivalent shell, i.e., $\forall k \in \{1, \ldots, n_{eq}\}$.

The information provided by JOREK is about the overall magnetic vector potential $\mathbf{A}$, rather than the one due to plasma currents. Hence, we have to "decouple" the vector potential due to sources in our different domains, i.e., $\mathbf{A}_{in} = \mathbf{A} - \mathbf{A_{ext}}$,

$$\int_{V_{eq}} \mathbf{w_k} \cdot (\mathbf{A} - \mathbf{A_{ext}}) \mathrm{d}V = \sum_{j=1}^{n_{eq}} I_{eq,j} \int_{V_{eq}} \mathbf{w_k}(\mathbf{x}) \cdot \frac{\mu_0}{4\pi} \int_{V_{eq}} \frac{\mathbf{w_j}(\mathbf{x}')}{|\mathbf{x} - \mathbf{x}'|} \mathrm{d}V' \mathrm{d}V. \quad (16)$$

Equation (16) highlights that the tangent component of the magnetic vector potential is the only information retained to evaluate the equivalent currents. While $\mathbf{A_{ext}}$ is calculated completely within CARIDDI as a function of the external currents, the magnetic vector potential tangent to the interface is given in the JOREK representation

$$\mathbf{A} = \sum_{j=1}^{n_{bnd}} \psi_j \lambda_j \nabla \varphi + \sum_{j=1}^{n_{bnd}} A_{\theta,j} \lambda_j \nabla \theta, \quad (17)$$

where n_{bnd} is the overall number of degrees of freedom per scalar field at the JOREK boundary. Here, λ_j are the usual JOREK basis functions given by the Cartesian product of Bezier curves in the poloidal plane and trigonometric functions along the toroidal angle. In matrix form, Eq. (15) is written as

$$\underline{\underline{H_\varphi}}\, \underline{\psi} + \underline{\underline{H_\theta}}\, \underline{A_\theta} - \underline{\underline{M_{eq,w}}}\, \underline{I_w} = \underline{\underline{L_{eq}}}\, \underline{I_{eq}}, \quad (18)$$

where

$$(H_\varphi)_{k,j} = \int_{V_{eq}} \mathbf{w_k} \cdot \nabla \varphi \lambda_j \mathrm{d}V, \quad (19)$$

$$(H_\theta)_{k,j} = \int_{V_{eq}} \mathbf{w_k} \cdot \nabla \theta \lambda_j \mathrm{d}V, \quad (20)$$

$$(M_{eq,w})_{k,j} = \int_{V_{eq}} \mathbf{w_k}(\mathbf{x}) \cdot \frac{\mu_0}{4\pi} \int_{V_c} \frac{\mathbf{w_j}(\mathbf{x}')}{|\mathbf{x} - \mathbf{x}'|} \mathrm{d}V' \mathrm{d}V, \quad (21)$$

$$(L_{eq})_{k,j} = \int_{V_{eq}} \mathbf{w_k}(\mathbf{x}) \cdot \frac{\mu_0}{4\pi} \int_{V_{eq}} \frac{\mathbf{w_j}(\mathbf{x}')}{|\mathbf{x} - \mathbf{x}'|} \mathrm{d}V' \mathrm{d}V. \quad (22)$$

It is important to stress here that coupling CARIDDI to the reduced MHD JOREK models, we neglect the poloidal component of the magnetic vector potential tangent to the boundary, i.e., $\underline{A_\theta}$ in Eq. (18). The equivalent current resulting from inversion of Eq. (18) is anyway consistent with the reduced MHD approximation: it will provide a poloidal magnetic field tangent to the boundary, which is exactly $-(1/r)\partial\psi_{in}/\partial n$ plus a term that will cancel out the magnetic field contribution from the A_θ component generated from the external currents.

The poloidal magnetic field tangent to the boundary due to equivalent plasma currents can be evaluated via the Biot–Savart matrix at specified points $\mathbf{x_i}$ on the outer page to the JOREK boundary

$$\left(B'_{\theta,eq}\right)_{i,j} = \mathbf{i}_\theta(\mathbf{x_i}) \cdot \int_{V_{eq}} \frac{\mu_0}{4\pi} \mathbf{w_j}(\mathbf{x}') \times \nabla' \frac{1}{|\mathbf{x_i} - \mathbf{x}'|} \mathrm{d}V' \tag{23}$$

and then projected to the Bezier space in the same manner as for Eq. (12) to obtain $B_{\theta,eq}$. Note that we do not evaluate the magnetic field exactly at the JOREK boundary for Eqs. (12) and (23), but at an outward shifted surface (1 mm outside $+\partial V_{in}$), since the equivalent surface current provides a discontinuity of the magnetic field across the JOREK boundary. The equivalent surface current, as defined in (14), can only represent solenoidal current distributions inside the MHD domain. Thus, currents crossing the MHD domain boundary, e.g., halo currents, cannot be described within this framework. The necessary correction terms to accommodate these currents have to be identified and implemented. The self-consistent inclusion of halo currents is under investigation, and it will require to understand the role of the continuity of the normal component of the current density across the JOREK boundary, besides the eventual role of electrodes' potentials on the plasma.

D. Resulting formulation

Thanks to the equivalent current representation of plasma sources, the induced currents within structures can be evolved in time according to the following equation:

$$\underline{\underline{L_w^*}} \frac{\mathrm{d}}{\mathrm{d}t} \underline{I_w} + \underline{\underline{R_w}}\, \underline{I_w} + \underline{\underline{N_\varphi}} \frac{\mathrm{d}}{\mathrm{d}t} \underline{\psi} + \underline{\underline{N_\theta}} \frac{\mathrm{d}}{\mathrm{d}t} \underline{A_\theta} = \underline{0}, \tag{24}$$

where based on definitions (19)–(22), we have introduced

$$\begin{aligned} &(a) \quad \underline{\underline{L_w^*}} = \underline{\underline{L_w}} - \underline{\underline{M_{w,eq}}}\, \underline{\underline{L_{eq}}}^{-1} \underline{\underline{M_{eq,w}}}, \\ &(b) \quad \underline{\underline{N_\varphi}} = \underline{\underline{M_{w,eq}}}\, \underline{\underline{L_{eq}}}^{-1} \underline{\underline{H_\varphi}}, \\ &(c) \quad \underline{\underline{N_\theta}} = \underline{\underline{M_{w,eq}}}\, \underline{\underline{L_{eq}}}^{-1} \underline{\underline{H_\theta}}. \end{aligned} \tag{25}$$

Equation (24) is obtained from the circuit equation for external currents (7), plugging expression (18) for equivalent plasma currents. Notice that $\underline{\underline{L_w^*}}$ can be interpreted as the conductive structures inductance matrix modified to account for the presence of a superconducting shell, which keeps constant the magnetic flux in correspondence of the JOREK boundary. On the other hand, induced voltages in passive structures due to magnetic flux variations at the JOREK boundary are provided by the matrices $\underline{\underline{N_\varphi}}$ and $\underline{\underline{N_\theta}}$. The magnetic field tangent to the JOREK boundary can be finally assigned in terms of external currents and magnetic vector potential. For example, for the tangent component of the poloidal magnetic field

$$\underline{B_\theta} = \underline{\underline{B_{\theta,w}^*}}\, \underline{I_w} + \underline{\underline{C_{\theta,\varphi}}}\, \underline{\psi} + \underline{\underline{C_{\theta,\theta}}}\, \underline{A_\theta}, \tag{26}$$

where

$$\begin{aligned} &(a) \quad \underline{\underline{B_{\theta,w}^*}} = \underline{\underline{B_{\theta,w}}} - \underline{\underline{B_{\theta,eq}}}\, \underline{\underline{L_{eq}}}^{-1} \underline{\underline{M_{eq,w}}}, \\ &(b) \quad \underline{\underline{C_{\theta,\varphi}}} = \underline{\underline{B_{\theta,eq}}}\, \underline{\underline{L_{eq}}}^{-1} \underline{\underline{H_\varphi}}, \\ &(c) \quad \underline{\underline{C_{\theta,\theta}}} = \underline{\underline{B_{\theta,eq}}}\, \underline{\underline{L_{eq}}}^{-1} \underline{\underline{H_\theta}}. \end{aligned} \tag{27}$$

An equation similar to (26) can be set of course also for the toroidal magnetic field. Anyway, we do not need this boundary condition here, as we are interested exclusively in the reduced MHD models. This means as well that we will set to zero the matrices $\underline{\underline{H_\theta}}$, $\underline{\underline{N_\theta}}$ and $\underline{\underline{C_{\theta,\theta}}}$. The matrix $\underline{\underline{C_{\theta,\theta}}}$ is here evaluated exclusively to check the consistency of our equivalent surface current representation against analytical test cases in Sec. III. As for JOREK-STARWALL,[26] we solve once for all the generalized eigenvalue problem

$$\underline{\underline{L_w^*}}\, \underline{S_\lambda} = \lambda \underline{\underline{R_w}}\, \underline{S_\lambda}. \tag{28}$$

In the eigenvector basis $\underline{S}$, the evolution equation (24) becomes diagonal, allowing to easily invert the linear system whenever we change the time step Δt of the implicit scheme adopted.

III. THE VACUUM RESPONSE

In this formulation, the essential element to decouple the electromagnetic problem between the inner and the outer domain is clearly the equivalent surface current to the plasma, placed at the JOREK boundary. The equivalent surface current $\mathbf{k_{eq}}$ is supposed to produce exactly the same magnetic field as the plasma in the outer domain. The necessary condition for this assumption to be robust is that the discretization adopted for the equivalent shell captures enough details of the JOREK boundary itself and there are enough degrees of freedom to accurately represent JOREK basis functions at the computational boundary. We have three parameters to adapt the equivalent shell to the JOREK boundary: the number of elements to use within one JOREK boundary element along the poloidal angle $n_{sub,\theta}$, the number of elements to use along the toroidal angle n_φ, and the thickness of the equivalent shell d_{eq}. We show in this section the results obtained for hexahedra discretizations of the JOREK boundary. The mesh adopted for the equivalent shell is built via a simple algorithm:

- Each JOREK boundary element in the poloidal plane is subdivided into $n_{sub,\theta}$ equally spaced sub-elements. The resulting nodes serve as reference mean poloidal locations for the equivalent shell construction.
- The inner page and outer page reference poloidal locations are obtained moving these reference points of $-d_{eq}/2$ and $+d_{eq}/2$ along the normal direction to the JOREK boundary. The thickness of the equivalent shell is always taken well below the typical dimensions of tokamak problems (e.g., $d_{eq} = 0.1$ mm).
- The nodes obtained so far are replicated n_φ times toroidally.
- An incidence matrix is set up either for hexahedra or pentahedra elements.

The above algorithm is implemented directly within CARIDDI, and accepts n_φ, $n_{sub,\theta}$, and d_{eq} as input parameters. The code is modified to read the JOREK boundary information, to build the mesh for the equivalent shell and to compute all the matrices required later on in JOREK for advancing the external currents self-consistently in time.

Furthermore, an automatic test, which checks the accuracy of the *vacuum response* matrices $C_{\theta,\varphi}$ and $C_{\theta,\theta}$, is implemented within the code. In particular, the magnetic field produced by the equivalent currents to a tilted toroidal wire placed at the center of the JOREK domain is verified against analytical formulas. This test is useful to check that the discretization chosen for the equivalent shell is sufficient to correctly reproduce the plasma-induced magnetic field (i.e., the parameters n_φ and $n_{sub,\theta}$ were tuned correctly). The automatic test procedure is used in this section to perform some sensitivity scans on a sample ASDEX Upgrade (AUG) like geometry, made of 50 poloidal JOREK boundary elements, i.e., $n_{bnd} = 50$.

We first investigate the sensitivity with respect to the integration precision for the matrices $\underline{\underline{L}}_{eq}$ (22) and $\underline{\underline{B}}_{eq}$ (23). For this scan, we fix the equivalent shell, considering eight poloidal subdivisions per JOREK boundary element and 90 elements along the toroidal angle (i.e., $n_{sub,\theta} = 8$, $n_\varphi = 90$). Even for the relatively small aspect ratio of AUG, these elements are strongly elongated in toroidal direction, i.e., the edges parallel to $\nabla\varphi$ are much longer than the edges parallel to $\nabla\theta$ ($h_\theta/h_\varphi \simeq 0.14$). Hence, the computation of $\underline{\underline{L}}_{eq}$ and $\underline{\underline{B}}_{eq}$ is intuitively more sensitive to the number of integration points in the toroidal direction. We quantify this dependence here in Fig. 2, where we show the Root Mean Square Error (RMSE) for the sine component of the first harmonic of the magnetic field. The RMSE can indeed be defined separately for each harmonic, comparing against the Fourier coefficients of the reference magnetic field evaluated via analytical formulas. The formal definition, for example, for the sine component of the kth harmonic, is

$$RMSE_{\sin,k} = \frac{\sqrt{\frac{1}{N_\theta}\sum_i \left(B_{ref,\sin,k}(r_i,z_i) - B_{\sin,k}(r_i,z_i)\right)^2}}{\sqrt{\frac{1}{N_\theta}\sum_i B_{ref,\sin,k}(r_i,z_i)^2}}. \quad (29)$$

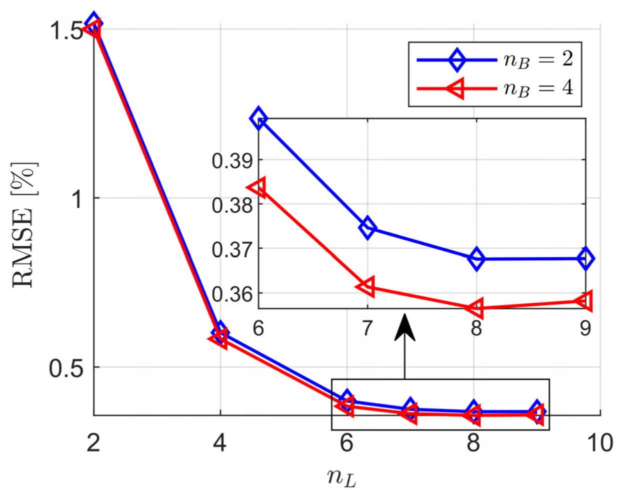

FIG. 2. *RMSE in the computation via equivalent currents of the magnetic field B_θ generated by a* tilted toroidal wire ($n = 1$ sin component). Sensitivity scan with respect to the number of Gauss points used along the toroidal direction for the computation of $\underline{\underline{L}}_{eq}$ (n_L) and the computation of $\underline{\underline{B}}_{\theta,eq}$ (n_B).

Note from Fig. 2 that the scheme is generally more sensitive to the integration precision of the inductance matrix L_{eq}, rather than the Biot–Savart matrix $B_{\theta,eq}$. This is not surprising as we have to invert the inductance matrix in order to define the response matrices $C_{\theta,\varphi}$ and $C_{\theta,\theta}$.

In Fig. 3, we show further results of our sensitivity scan. The RMSE generally improves increasing the poloidal discretization of the equivalent shell, i.e., increasing the number of poloidal subdivisions on the JOREK boundary element $n_{sub,\theta}$. In general, especially for higher-order toroidal harmonics, the accuracy will improve also increasing the number of elements along the toroidal angle n_φ, as is shown in Fig. 3(b). Indeed, by increasing the toroidal resolution, we keep

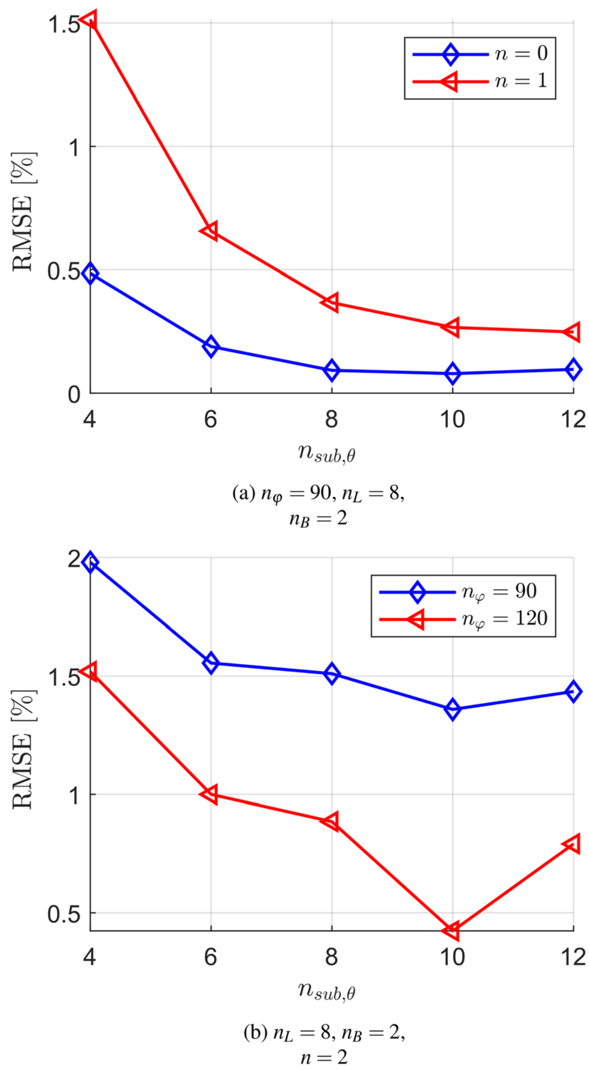

FIG. 3. Scan of the RMSE for the poloidal magnetic field computed by the equivalent currents to a tilted toroidal wire for different poloidal discretizations of an AUG computational boundary ($n_{bnd} = 50$). In panel (a), we show the RMSE for the $n = 0$ and $n = 1$ component; in panel (b), we show the RMSE for the $n = 2$ component, also for different levels of toroidal discretization.

decreasing the difference between the toroidal arcs and the respective chords by which we are approximating them. The error estimates which we present in Figs. 2 and 3 do not account for the error we introduce evaluating the magnetic field at a surface, which is slightly shifted outwards as compared to the JOREK boundary (i.e., 1 mm away from the boundary). The error related to this approximation does not exceed 0.15 % in the above tests.

IV. A VDE TEST CASE

In this section, we validate the efficacy of our coupling strategy via a three-way comparison. We compare the simulations for a vertical displacement event (VDE) in AUG as computed in JOREK-CARIDDI, JOREK-STARWALL,[26] and CarMa0NL.[8] While JOREK-STARWALL and JOREK-CARIDDI share the same plasma model, JOREK-CARIDDI and CarMa0NL share the same model for external conductors. In particular, we implement in CARIDDI a simplified version of wall structures and Passive Stabilizing Loop (PSL), similar to the available STARWALL model for AUG. Two independent loops, each configured by several thin bands with the same current, are set up in STARWALL. The CARIDDI model also consists of two independent loops, although this time the conductors are bulky. CarMa0NL implements an *evolutionary equilibrium model* for the plasma, which is forced to be axisymmetric. The mass-less assumption made in *CarMa0NL* is satisfactory in general for vertical stability studies,[49] and it is sufficient for this case in particular, as we shall see later in this section. As first step, the same MHD equilibrium condition is reproduced in the three codes. Notice that, besides the plasma model is precisely the same, the JOREK-STARWALL and the JOREK-CARIDDI free-boundary equilibria can be slightly different due to the different representation adopted for the equivalent currents to the plasma. The temperature and density profiles in JOREK are tuned in a way to fit the p' and FF' equilibrium profiles set up in CarMa0NL. This MHD equilibrium condition is taken as initial condition for a non-linear simulation in each code. Since CarMa0NL is able to capture only the axisymmetric evolution of the plasma column, we consider exclusively the $n = 0$ mode also in JOREK-STARWALL and JOREK-CARIDDI for this comparison. The VDE is triggered forcing a current kick in the vertical control circuit to produce a well-defined initial perturbation. In CarMa0NL, the plasma current and the equilibrium profiles are kept strictly constant throughout the evolution. Thus, we activate an artificial current source term in JOREK to keep the equilibrium profiles virtually constant throughout the evolution. The evolution of the vertical position of the plasma magnetic axis in JOREK-STARWALL, JOREK-CARIDDI, and CarMa0NL is reported in Fig. 4.

The growth rate of the instability, as estimated via an exponential fit from the non-linear simulations, is in good agreement between the three codes, see Fig. 5. There the difference between the JOREK-STARWALL and the JOREK-CARIDDI growth rates is always below 2%. The small differences in the overall evolution may be attributed in part to the different *equivalent current* representation, and in part to the different models of the PSLs. These conductors are indeed very close to the plasma: their eddy currents provide the dominant contribution to slowing down the vertical plasma motion in comparison with the no-wall limit. To provide an idea regarding the importance of coherent PSL modeling for the growth rate estimation, we show the magnetic axis position vs the upper and lower PSL currents in Fig. 6. This figure validates essentially also the *mass-less* approximation adopted in CarMa0NL, showing that the relation between external

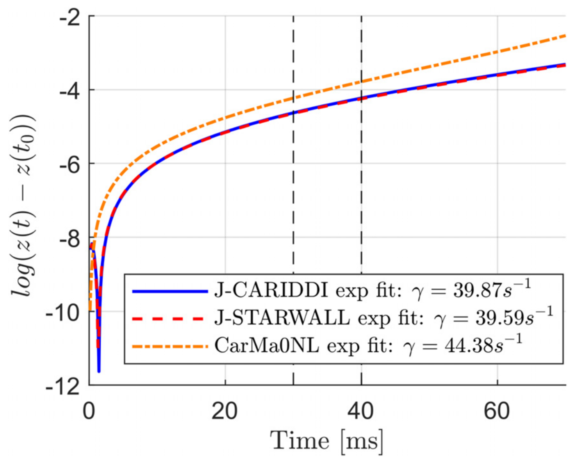

FIG. 4. Vertical displacement evolution for an AUG test case in semi-log scale. The growth rate indicated in the legend is evaluated via an exponential fit in the highlighted time window.

currents and vertical position looks like an equilibrium characteristic, although slightly different, also in the JOREK simulations. This difference and the increasing error with time of the vertical growth rate from initially 1% between CarMa0NL and the JOREK is a result from the different physics models. The definition of ψ_N changes with the movement into the wall. While the ψ_N profiles are kept exactly constant in CarMa0NL, the current source in JOREK does not strictly enforce this condition, and the small changes over time lead to the difference in growth rates. Furthermore, the plasma current slightly varies in JOREK, while it is kept fixed in the CarMa0NL simulation.

V. A TEARING MODE TEST CASE

In this section, a large aspect ratio tearing mode test case is considered to validate the code coupling for non-axisymmetric harmonics.

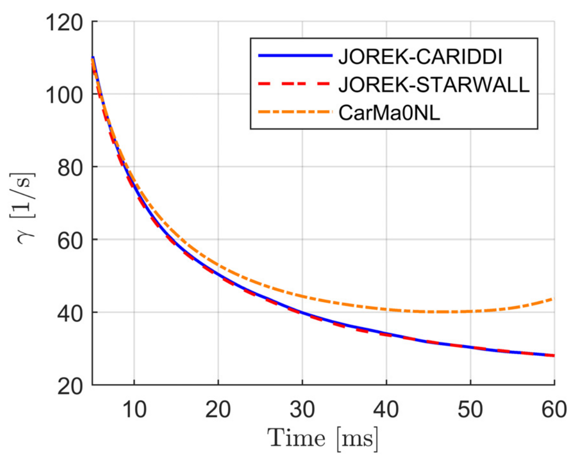

FIG. 5. Evolution of the growth rates for the axisymmetric VDE, as estimated by exponential fit of the simulated data. A time interval of 10 ms is adopted for the fitting: the time in the abscissa indicates the first time instant for the exponential fit.

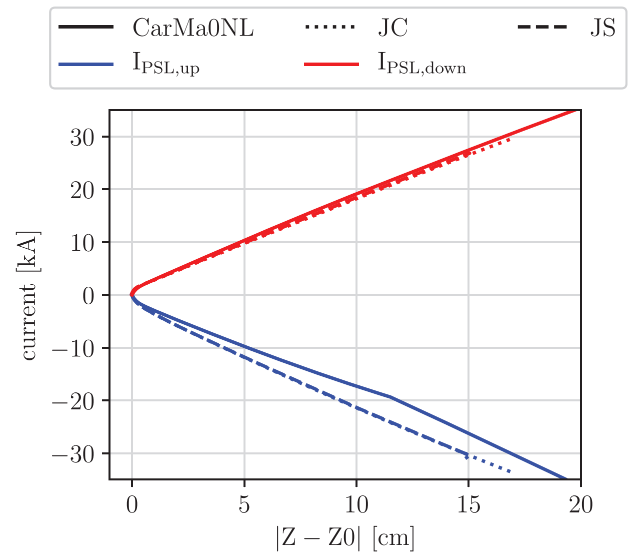

FIG. 6. Evolution of the current in the lower ($I_{PSL,down}$) and upper ($I_{PSL,up}$) PSL with the displacement of the plasma for CarMa0NL, JOREK-CARIDDI (JC), and JOREK-STARWALL (JS) in an axisymmetric VDE simulation.

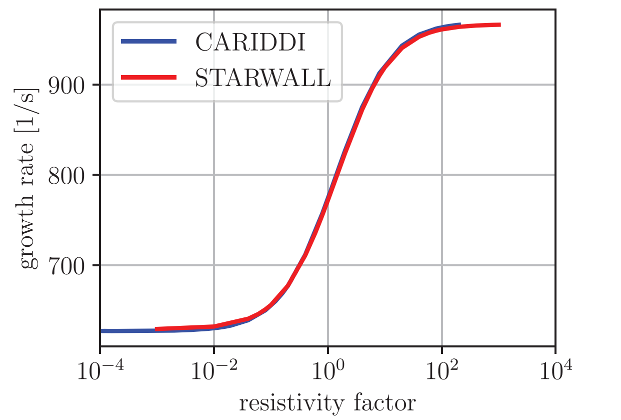

FIG. 7. The nominal wall resistivity of $5 \times 10^{-7}\,\Omega\,$m was scanned to compare the $n = 1$ growth rates of the tearing mode from the ideal wall limit to the no-wall limit.

The no-pressure equilibrium considered is unstable against a 2/1 tearing mode. The MHD computational boundary and the initial MHD equilibrium are configured in such a way that the $q = 2$ surface is relatively close to the wall, to amplify the effect of the interaction. The circular plasma with a major radius R of 10 m and a minor radius a of 1 m is surrounded by a toroidally symmetric wall with a circular cross section and a minor radius of 1.1 m. The coupling surface is discretized in CARIDDI via pentahedra similar to the STARWALL triangles ($n_\varphi = 120$, $n_{sub,\theta} = 10$). Also, the wall is discretized via pentahedra, again to mimic the STARWALL discretization. A nominal resistivity of $5 \times 10^{-7}\,\Omega{\cdot}$m was chosen for the wall in CARIDDI. Taking into account the wall thickness of 5 mm, the respective thin wall resistivity in STARWALL $\eta_{\mathrm{wall,thin}}$ is $1 \times 10^{-4}\,\Omega$. The wall resistivity is scanned in order to assess the growth rate variation of the tearing mode from the ideal-wall limit to the no-wall limit. Figure 7 shows that the growth rate of the tearing mode matches with differences below 1% over several orders of magnitude in the wall resistivity.

VI. EFFECTS OF 3D CONDUCTING STRUCTURES ONTO THE PLASMA DYNAMICS

The three-dimensional features of conductors surrounding the plasma break the axisymmetry of the outer eddy current problem and allow the coupling of different toroidal harmonics even during the linear phase of the plasma evolution. This circumstance was observed already in Ref. 50, where the dispersion relation for kink modes in tokamaks was studied in presence of a wall with toroidally varying electrical resistance or thickness. In Ref. 51, the details of the 3D structures were found to be important for the correct prediction of the growth rate of resistive wall modes occurring in RFX-mod experiments. The integrated model developed here will allow to extend those analysis to non-linear regimes, hence to study the effect of 3D conductors also in critical tokamak transient phases. Wide interest in the literature has been reserved for example to the raise of lateral forces in tokamak walls during disruptions,[52,53] but there are no analyses available yet based on simultaneous 3D modeling of plasma and structures.

In this section, we explore the effect of the wall geometry in two different ways: (1) studying the coupling of distinct $n > 0$ MHD modes due to a different number of port openings, (2) analyzing how the $n = 0$ unstable mode in such a configuration triggers $n > 0$ unstable modes due to the 3D deviations of the reaction current.

We first investigate the coupling between $n > 0$ modes, considering an MHD equilibrium, which is again unstable with respect to a 2/1 tearing mode in the AUG-like geometry under analysis. Note that $n = 2$ is linearly stable in this configuration. We consider equally spaced holes at the bottom of the device, whose poloidal span is indicated in blue in Fig. 9. The toroidal span of each hole is 30°. The PSL is here excluded from the model. In particular, we investigate the properties of modes coupling by considering a different number of holes along the torus, $n_{holes} = \{0, 1, 2, 3, 4, 6, 8\}$. Figure 8 shows how the evolution of non-axisymmetric magnetic energies is influenced by the

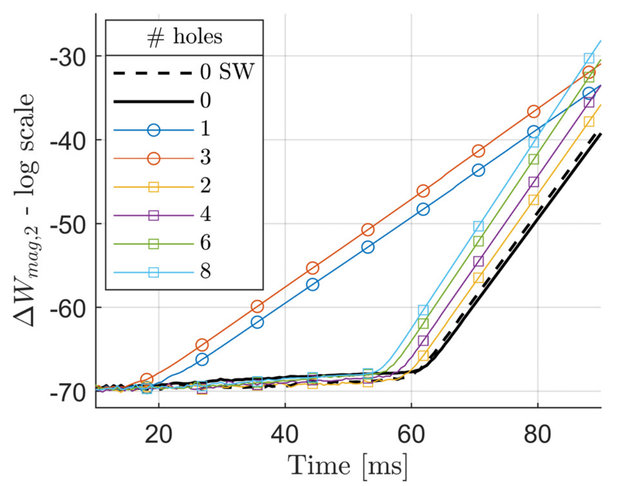

FIG. 8. The $n = 2$ magnetic energy evolution for the AUG tearing mode test case, using a different number of equally spaced holes along the toroidal angle.

TABLE I. Growth rate (*rad/s*) for the $n=1$ and $n=2$ unstable modes of the ASDEX tearing mode test case varying the number of holes placed along the toroidal angle.

n_{holes}	0	1	2	3	4	6	8
$n=1$	509.5	518.7	532.9	534.4	541.8	559.7	573.0
$n=2$	1019.0	523.7	1065.9	535.9	1083.4	1119.0	1144.0

presence of holes in the originally axisymmetric structures. There we also illustrate the evolution for an axisymmetric wall in a JOREK-STARWALL simulation, to further support our previous benchmark. We include exclusively the toroidal harmonics $n=1$ and $n=2$ in the JOREK simulation, independently on the number of ports we include in the wall model.

The growth rate of the $n=1$ unstable mode increases with the number of ports placed along the toroidal angle, since each hole represents an obstacle to the flow of a reaction eddy current, see details in Table I. For the cases $n_{holes} = \{2, 4, 6, 8\}$, the conductors do not determine any external coupling between the $n=1$ and $n=2$ magnetic fields, as for the axisymmetric case ($n_{holes}=0$). In these cases, the $n=2$ mode becomes unstable due to non-linear coupling within the plasma. In particular, the $n=2$ instability is excited when the $n=1$ magnetic energy overcomes the same threshold value. Depending on how much time is required to reach this threshold value, we observe different onset times for the $n=2$ unstable mode in Fig. 8. This type of non-linear coupling determines a growth rate of the $n=2$ unstable mode, which is twice as big as the corresponding growth rate of the $n=1$ unstable mode, again see details in Table I. On the other hand, for the cases $n_{holes} = \{1, 3\}$, direct mutual coupling of the $n=1$ and $n=2$ modes takes place via the wall structures. Correspondingly, we observe an earlier onset of the $n=2$ instability, which is driven by the $n=1$ instability. In these cases, the growth rate of the $n=2$ magnetic energy is essentially the same as the growth rate of the $n=1$ magnetic energy. The quite clear distinction we observe between the two groups of simulations $n_{holes} = \{2, 4, 6, 8\}$ and $n_{holes} = \{1, 3\}$ is clearly related to the assumption of considering only the $n=1$ and $n=2$ toroidal harmonics in the plasma model. Accurate account of further harmonics in the plasma could have resulted in an indirect linear coupling of the $n=1$ and $n=2$ modes via higher harmonics also for the $n_{holes} = \{2, 4, 6, 8\}$ cases. We postpone this analysis to future studies.

Furthermore, we consider the coupling between $n=0$ and higher modes due to the port openings. This time, we examine the effect of different port openings at a single toroidal location. In particular, three different cases are considered both in CARIDDI and STARWALL: (a) a toroidally symmetric wall, (b) an axisymmetric wall with a single port at the midplane, (c) an axisymmetric wall with a single port at the bottom of the machine. The ports, centered at $\varphi = -90°$, have a toroidal extension of 33.75°, and their poloidal extension is shown in Fig. 9. The resistance of the PSL is artificially increased to enhance the effects of the 3D features on the plasma evolution. We take as basis the physics model presented in Ref. 54. To include 3D MHD effects, the harmonics $n = \{1, 2, 3\}$ are included in JOREK after a brief axisymmetric phase carried out to establish equilibrium flows. When the additional harmonics are added, a downward VDE is initiated by a kick from the control coils similar to the case presented in Sec. IV. Figure 10 displays the evolution of the vertical position of the magnetic axis, of the edge safety factor $q_{95} = q(\psi_n = 0.95)$, and of the $n=1$ and $n=2$ magnetic energies. In the presence of non-axisymmetric structures, the perturbation of the higher mode numbers is defined by the port: the energy of $n > 0$ modes in JOREK-CARIDDI and JOREK-STARWALL are immediately excited to the same finite amplitude when the current in control coils is perturbed. In the case of the axisymmetric wall, the current kick does not produce any $n > 0$ variation, and we do not encounter any appreciable magnetic energy variation of higher-order modes until we get into the non-linear phase of the plasma evolution. The cases with a port have a slightly larger vertical growth rate than the axisymmetric wall case [see Figs. 10(a) and 10(b)], as the eddy currents are perturbed, although structures are relatively far and most of the stabilizing current flows at the high field side of the machine, where no ports are located. The additional perturbation by the port triggers the MHD activity that leads to the Thermal Quench (TQ) at an earlier point in time. This can be due to the coupling of different modes leading to a faster growth of the energies as well as to a reduced stabilization of the modes due to the perturbed eddy current paths.

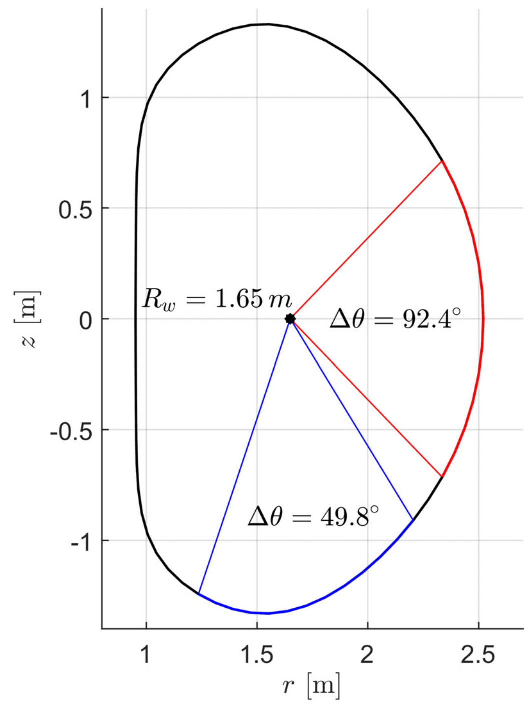

FIG. 9. Ports around the AUG wall, used for the study of mode coupling via conductors' reaction field.

Figure 11 shows how the wall currents establish in the region around the hole, which leads to the coupling of toroidal harmonics. Here, the toroidal current density is represented by the color coding and the arrows represent the amplitude and direction of the total current density.

VII. CONCLUSIONS AND FUTURE WORK

In this manuscript, we addressed the coupling of an extended non-linear MHD code[1] with a fully 3D volumetric model of surrounding conductors[38] for tokamak applications. The resulting JOREK-

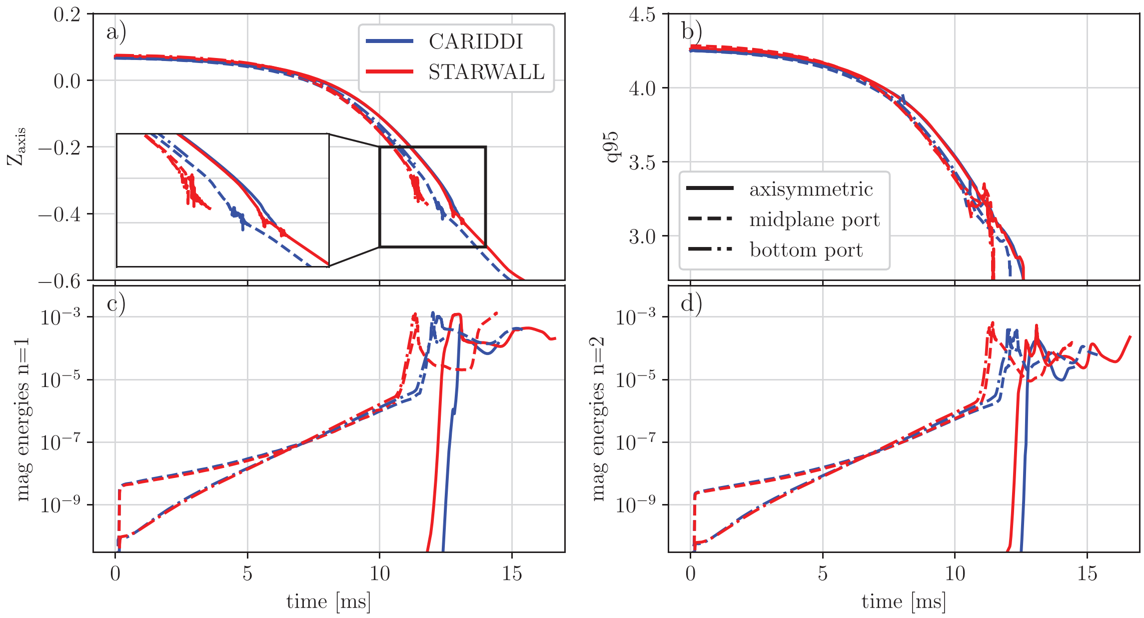

FIG. 10. The evolution of the (a) vertical displacement, (b) edge safety factor q_{95}, (c) $n = 1$ magnetic energy, and (d) $n = 2$ magnetic energy is shown for the 3D VDE in presence of an axisymmetric wall and a wall with a localized hole either at the midplane or at the bottom of the device. It can be seen that the presence of holes determines: higher vertical growth rate; solicitation of the $n > 0$ magnetic energies during the current kick in the vertical control circuit; earlier TQ onset at a larger value of q_{95}.

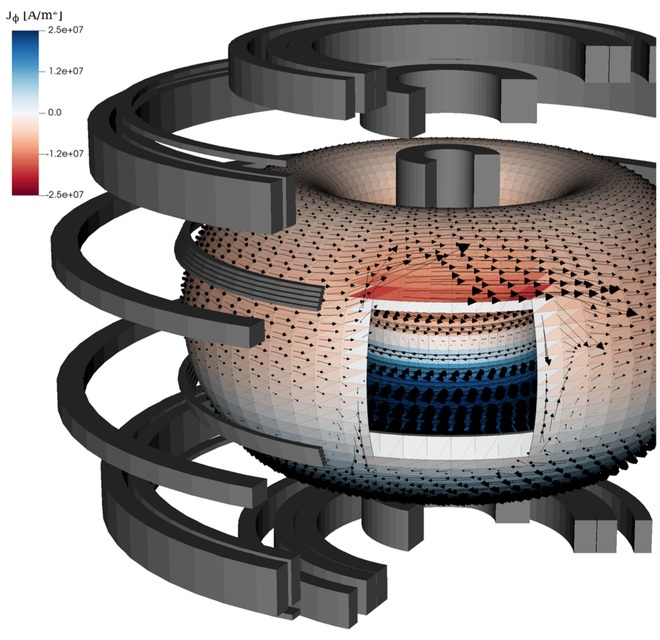

FIG. 11. Current distribution at a certain time instant of the 3D VDE simulation for the AUG-like geometry. The colormap refers to the toroidal current density, while arrows represent the overall current density field. The Poloidal Field (PF) coils of AUG are shown in gray. Notice as the presence of the hole determines a deviation of the current density distribution from a purely axisymmetric reaction current.

CARIDDI integrated model is the first numerical tool capable of simulating 3D non-linear MHD plasmas in self-consistent interaction with eddy currents in 3D volumetric conductors. This tool will be useful for studying tokamak disruptions and their effect on conductors, besides resistive wall modes during the non-linear phase of evolution.

One limitation of the coupling scheme presented is given by the reduced MHD ansatz, $\mathbf{A} = \psi \nabla \varphi$, which does not allow us to describe the poloidal plasma currents in a completely self-consistent way. We have delineated how to extend the scheme to more general *full MHD* models in Sec. II and implementation of the free-boundary option into the full MHD models will be addressed in future work. Another limitation, we did not account for yet, is the presence of shared currents between plasma and conductors. Since these multi-domain currents, also known as *halo currents*, are crucial in the description of fast plasma quenches,[12] the possibility to include halo currents in the present scheme is already under investigation. In this more complicate case, the definition of *plasma* equivalent current has to be specified further: the current density distribution within the MHD domain is not solenoidal on its own, the solenoidality is preserved only in the whole domain, including plasma and conductors. Another future extension is related to stellarator applications, where the control surface itself becomes non-axisymmetric.

We have shown that the plasma magnetic field in the outer domain can be represented up to an error of 0.2% with the present scheme, and several improvements are under investigation, including an approach to increase the accuracy of the shell inductance calculation and a method to exploit the axi-symmetry of the JOREK boundary.[55] Several benchmarks have been carried out to assess the coupling. A three-way benchmark of an axisymmetric VDE test case between

JOREK-CARIDDI, JOREK-STARWALL and CarMa0NL was performed to validate the JOREK-CARIDDI model. The STARWALL and CARIDDI description in a simplified geometry showed that the vertical growth rate evolve in the same way, while γ in CarMa0NL deviates about 10%, after better agreement in the initial phase, due to the different plasma model.

The coupling between the higher-order MHD harmonics and an axisymmetric wall was assessed by a tearing mode test case in the large-aspect-ratio limit. The growth rates calculated by JOREK-STARWALL and JOREK-CARIDDI match very well from the no-wall up to the ideal wall limit.

The main feature of JOREK-CARIDDI is the coupling between realistic 3D structures and the non-axisymmetric plasma model. The efficacy in the description of 3D effects was assessed by a tearing mode test case for an AUG-like geometry, considering a different number of similar port openings in the wall equally spaced along the toroidal angle. Our model captures the coupling of magnetic field toroidal harmonics via external structures, consistently with the toroidal periodicity of the deviation introduced in the originally axisymmetric wall. The analysis raises the important question that for realistic applications, it may be necessary to tune the number of toroidal harmonics to include in the plasma model according to the toroidal periodicity of external conductors. As last case, a hot VDE evolution up to the thermal quench in the presence of a port in the wall, again for an AUG-like geometry, was considered. The vertical growth rate increases slightly due to the deviation of the stabilizing currents. Also, the initial perturbation of the $n > 0$ modes in the plasma is generated from the non-axisymmetric wall currents generated during the axisymmetric current kick in the vertical control coils. These asymmetries lead to an earlier onset of the thermal quench.

The benchmarks provided confidence in the newly established JOREK-CARIDDI model, which is now ready for physics applications: realistic disruption simulations including load assessment, thorough studies of the interaction between rotating modes and conductive structures, and direct comparison of simulations with experiments via detailed magnetic diagnostics modeling.

Furthermore, improvements are under development to allow for the treatment of complex full-torus conducting structures, where the dimension of the space of external currents can become elevated (e.g., $> 500k$ degrees of freedom). We are exploring both compression techniques for the conductors response matrices[56] and investigating how to exploit the approximate n-fold symmetry of most tokamak devices in this context.[57]

ACKNOWLEDGMENTS

The authors wish to thank Professor G. Huysmans, Dr. F. Cipolletta, Dr. F. Vannini, and Mr. R. Sparago for the many fruitful discussions. Moreover, the authors wish to thank Dr. S. Mochalskyy for his support in setting up the parallel I/O of interface matrices.

This work has been carried out within the framework of the EUROfusion Consortium, funded by the European Union via the Euratom Research and Training Programme (Grant Agreement No. 101052200–EUROfusion). Views and opinions expressed are however those of the author(s) only and do not necessarily reflect those of the European Union or the European Commission. Neither the European Union nor the European Commission can be held responsible for them.

This work was partially carried out using EUROfusion High Performance Computer Marconi-Fusion through EUROfusion funding.

ITER is the Nuclear Facility INB No. 174. This paper explores physics processes during the plasma operation of the tokamak when disruptions take place; nevertheless, the nuclear operator is not constrained by the results presented here. The views and opinions expressed herein do not necessarily reflect those of the ITER Organization.

This work was supported in part by Italian MUR (PRIN Grant No. 20177BZMAH).

AUTHOR DECLARATIONS

Conflict of Interest

The authors have no conflicts to disclose.

Author Contributions

Nicola Isernia: Conceptualization (equal); Data curation (equal); Formal analysis (equal); Investigation (equal); Methodology (equal); Software (equal); Validation (equal); Visualization (equal); Writing – original draft (equal); Writing – review & editing (equal). **Nina Schwarz**: Conceptualization (equal); Data curation (equal); Formal analysis (equal); Investigation (equal); Methodology (equal); Software (equal); Supervision (equal); Validation (equal); Visualization (equal); Writing – original draft (equal); Writing – review & editing (equal). **F. J. Artola**: Conceptualization (equal); Methodology (equal). **Salvatore Ventre**: Software (equal). **Matthias Hoelzl:** Conceptualization (equal); Supervision (equal); Writing – original draft (equal); Writing – review & editing (equal). **Guglielmo Rubinacci**: Conceptualization (equal); Supervision (equal). **Fabio Villone:** Conceptualization (equal); Supervision (equal).

DATA AVAILABILITY

The data that support the findings of this study are available from the corresponding author upon reasonable request.

REFERENCES

[1] M. Hoelzl, G. T. A. Huijsmans, S. J. P. Pamela, M. Bécoulet, E. Nardon, F. J. Artola, B. Nkonga, C. V. Atanasiu, V. Bandaru, A. Bhole, D. Bonfiglio, A. Cathey, O. Czarny, A. Dvornova, T. Fehér, A. Fil, E. Franck, S. Futatani, M. Gruca, H. Guillard, J. W. Haverkort, I. Holod, D. Hu, S. K. Kim, S. Q. Korving, L. Kos, I. Krebs, L. Kripner, G. Latu, F. Liu, P. Merkel, D. Meshcheriakov, V. Mitterauer, S. Mochalskyy, J. A. Morales, R. Nies, N. Nikulsin, F. Orain, J. Pratt, R. Ramasamy, P. Ramet, C. Reux, K. Särkimäki, N. Schwarz, P. S. Verma, S. F. Smith, C. Sommariva, E. Strumberger, D. C. van Vugt, M. Verbeek, E. Westerhof, F. Wieschollek, and J. Zielinski, "The JOREK non-linear extended MHD code and applications to large-scale instabilities and their control in magnetically confined fusion plasmas," Nucl. Fusion **61**, 065001 (2021).

[2] S. C. Jardin and D. A. Larrabee, "Feedback stabilization of rigid axisymmetric modes in tokamaks," Nucl. Fusion **22**, 1095–1098 (1982).

[3] D. A. Humphreys and I. H. Hutchinson, "Filament-circuit model analysis of Alcator C-MOD vertical stability," Technical Report No. PFC/JA-89-28 (Plasma Fusion Center, Massuchetts Institute of Technology, 1989).

[4] E. A. Lazarus, J. B. Lister, and G. H. Neilson, "Control of the vertical instability in tokamaks," Nucl. Fusion **30**, 111–141 (1990).

[5] D. J. Ward, S. C. Jardin, and C. Z. Cheng, "Calculations of axisymmetric stability of tokamak plasmas with active and passive feedback," J. Comput. Phys. **104**, 221–240 (1993).

[6]R. Albanese and F. Villone, "The linearized CREATE-L plasma response model for the control of current, position and shape in tokamaks," Nucl. Fusion **38**, 723–738 (1998).
[7]R. Khayrutdinov and V. Lukash, "Studies of plasma equilibrium and transport in a tokamak fusion device with the inverse-variable technique," J. Comput. Phys. **109**, 193–201 (1993).
[8]F. Villone, L. Barbato, S. Mastrostefano, and S. Ventre, "Coupling of nonlinear axisymmetric plasma evolution with three-dimensional volumetric conductors," Plasma Phys. Controlled Fusion **55**, 095008 (2013).
[9]D. J. Ward and A. Bondeson, "Stabilization of ideal modes by resistive walls in tokamaks with plasma rotation and its effect on the beta limit," Phys. Plasmas **2**, 1570–1580 (1995).
[10]M. S. Chu and M. Okabayashi, "Stabilization of the external kink and the resistive wall mode," Plasma Phys. Controlled Fusion **52**, 123001 (2010).
[11]E. J. Strait, T. S. Taylor, A. D. Turnbull, J. R. Ferron, L. L. Lao, B. Rice, O. Sauter, S. J. Thompson, and D. Wróblewski, "Wall stabilization of high beta tokamak discharges in DIII-D," Phys. Rev. Lett. **74**, 2483–2486 (1995).
[12]T. C. Hender, J. C. Wesley, J. Bialek, A. Bondeson, A. H. Boozer, R. J. Buttery, A. Garofalo, T. P. Goodman, R. S. Granetz, Y. Gribov, O. Gruber, M. Gryaznevich, G. Giruzzi, S. Günter, N. Hayashi, P. Helander, C. C. Hegna, D. F. Howell, D. A. Humphreys, G. T. A. Huysmans, A. W. Hyatt, A. Isayama, S. C. Jardin, Y. Kawano, A. Kellman, C. Kessel, H. R. Koslowski, R. J. L. Haye, E. Lazzaro, Y. Q. Liu, V. Lukash, J. Manickam, S. Medvedev, V. Mertens, S. V. Mirnov, Y. Nakamura, G. Navratil, M. Okabayashi, T. Ozeki, R. Paccagnella, G. Pautasso, F. Porcelli, V. D. Pustovitov, V. Riccardo, M. Sato, O. Sauter, M. J. Schaffer, M. Shimada, P. Sonato, E. J. Strait, M. Sugihara, M. Takechi, A. D. Turnbull, E. Westerhof, D. G. Whyte, R. Yoshino, H. Zohm, ITPA MHD, and Disruption and Magnetic Control Topical Group, "Chapter 3: MHD stability, operational limits and disruptions," Nucl. Fusion **47**, 128–202 (2007).
[13]R. Albanese, M. Mattei, and F. Villone, "Prediction of the growth rates of VDEs in JET," Nucl. Fusion **44**, 999–1007 (2004).
[14]S. L. Chen, F. Villone, B. J. Xiao, L. Barbato, Z. P. Luo, L. Liu, S. Mastrostefano, and Z. Xing, "3D passive stabilization of $n = 0$ MHD modes in EAST tokamak," Sci. Rep. **6**, 32440 (2016).
[15]F. Villone, Y. Liu, G. Ambrosino, and A. Pironti, "Effects of three-dimensional conducting structures on resistive wall modes," AIP Conf. Proc. **1069**, 221–230 (2008).
[16]Y. Liu, M. S. Chu, W. F. Guo, F. Villone, R. Albanese, G. Ambrosino, M. Baruzzo, T. Bolzonella, I. T. Chapman, A. M. Garofalo, C. G. Gimblett, R. J. Hastie, T. C. Hender, G. L. Jackson, R. J. L. Haye, M. J. Lanctot, Y. In, G. Marchiori, M. Okabayashi, R. Paccagnella, M. F. Palumbo, A. Pironti, H. Reimerdes, G. Rubinacci, A. Soppelsa, E. J. Strait, S. Ventre, and D. Yadykin, "Resistive wall mode control code maturity: progress and specific examples," Plasma Phys. Controlled Fusion **52**, 104002 (2010).
[17]V. Pustovitov, "Energy principle for the modes interacting with a resistive wall in toroidal systems," Nucl. Fusion **55**, 033008 (2015).
[18]W. Park, E. Belova, G. Fu, X. Tang, H. Strauss, and L. Sugiyama, "Plasma simulation studies using multilevel physics models," Phys. Plasmas **6**, 1796–1803 (1999).
[19]H. Strauss, A. Pletzer, W. Park, S. Jardin, J. Breslau, and L. Sugiyama, "MHD simulations with resistive wall and magnetic separatrix," Comput. Phys. Commun. **164**, 40–45 (2004).
[20]C. Sovinec, A. Glasser, T. Gianakon, D. Barnes, R. Nebel, S. Kruger, D. Schnack, S. Plimpton, A. Tarditi, and M. Chu, "Nonlinear magnetohydrodynamics simulation using high-order finite elements," J. Comput. Phys. **195**, 355–386 (2004).
[21]C. R. Sovinec and K. J. Bunkers, "Effects of asymmetries in computations of forced vertical displacement events," Plasma Phys. Controlled Fusion **61**, 024003 (2019).
[22]F. J. Artola, C. R. Sovinec, S. C. Jardin, M. Hoelzl, I. Krebs, and C. Clauser, "3D simulations of vertical displacement events in tokamaks: A benchmark of M3D-C1, NIMROD, and JOREK," Phys. Plasmas **28**, 052511 (2021).
[23]S. C. Jardin, J. Breslau, and N. Ferraro, "A high-order implicit finite element method for integrating the two-fluid magnetohydrodynamic equations in two dimensions," J. Comput. Phys. **226**, 2146–2174 (2007).
[24]J. Breslau, N. Ferraro, and S. Jardin, "Some properties of the M3D-C1 form of the three-dimensional magnetohydrodynamics equations," Phys. Plasmas **16**, 092503 (2009).
[25]N. M. Ferraro, S. C. Jardin, L. L. Lao, M. S. Shephard, and F. Zhang, "Multi-region approach to free-boundary three-dimensional tokamak equilibria and resistive wall instabilities," Phys. Plasmas **23**, 056114 (2016).
[26]M. Hoelzl, P. Merkel, G. T. A. Huysmans, E. Nardon, E. Strumberger, R. McAdams, I. Chapman, S. Günter, and K. Lackner, "Coupling JOREK and STARWALL codes for non-linear resistive-wall simulations," J. Phys.: Conf. Ser. **401**, 012010 (2012).
[27]F. J. Artola, "Free-boundary simulations of MHD plasma instabilities in tokamaks," Ph.D. thesis, Universitè Aix-Marseille, 2018.
[28]E. Strumberger and S. Günter, "Castor3d: Linear stability studies for 2d and 3d tokamak equilibria," Nucl. Fusion **57**, 016032 (2016).
[29]E. Strumberger and S. Günter, "Linear stability studies for a quasi-axisymmetric stellarator configuration including effects of parallel viscosity, plasma flow, and resistive walls," Nucl. Fusion **59**, 106008 (2019).
[30]J. Bialek, A. H. Boozer, M. E. Mauel, and G. A. Navratil, "Modeling of active control of external magnetohydrodynamic instabilities," Phys. Plasmas **8**, 2170–2180 (2001).
[31]A. Bondeson, G. Vlad, and H. Lütjens, "Resistive toroidal stability of internal kink modes in circular and shaped tokamaks," Phys. Fluids B **4**, 1889–1900 (1992.
[32]Y. Q. Liu, A. Bondeson, C. M. Fransson, B. Lennartson, and C. Breitholtz, "Feedback stabilization of nonaxisymmetric resistive wall modes in tokamaks. I. Electromagnetic model," Phys. Plasmas **7**, 3681–3690 (2000.
[33]P. Testoni and A. Portone, "Introduction and validation of the APEC code for the simulation of plasma equilibrium and evolution in the presence of 3-D passive structures," IEEE Trans. Magn. **56**, 1–4 (2020).
[34]A. Portone, F. Villone, Y. Liu, R. Albanese, and G. Rubinacci, "Linearly perturbed MHD equilibria and 3d eddy current coupling via the control surface method," Plasma Phys. Controlled Fusion **50**, 085004 (2008).
[35]M. Bonotto, Y. Q. Liu, F. Villone, L. Pigatto, and P. Bettini, "Expanded capabilities of the CarMa code in modeling resistive wall mode dynamics with 3-D conductors," Plasma Phys. Controlled Fusion **62**, 045016 (2020).
[36]G. T. A. Huysmans and O. Czarny, "MHD stability in X-point geometry: simulation of ELMs," Nucl. Fusion **47**, 659–666 (2007).
[37]O. Czarny and G. Huysmans, "Bézier surfaces and finite elements for MHD simulations," J. Comput. Phys. **227**, 7423–7445 (2008).
[38]R. Albanese and G. Rubinacci, "Integral formulation for 3d eddy-current computation using edge elements," IEE Proc., Part A: Phys. Sci., Meas. Instrum., Manage. Educ. Rev. **135**, 457 (1988).
[39]R. Albanese and G. Rubinacci, "Finite element methods for the solution of 3D eddy current problems," Adv. Imaging Electron Phys. **102**, 1–86 (1997).
[40]F. Cau, A. G. Chiariello, G. Rubinacci, V. Scalera, A. Tamburrino, S. Ventre, and F. Villone, "A fast matrix compression method for large scale numerical modelling of rotationally symmetric 3d passive structures in fusion devices," Energies **15**, 3214 (2022).
[41]F. Brezzi and C. Johnson, "On the coupling of boundary integral and finite element methods," Calcolo **16**, 189–201 (1979).
[42]C. Johnson and J.-C. Nédélec, "On the coupling of boundary integral and finite element methods," Math. Comput. **35**, 1063–1079 (1980).
[43]K. Lackner, "Computation of ideal MHD equilibria," Comput. Phys. Commun. **12**, 33–44 (1976).
[44]B. J. Braams, "The interpretation of tokamak magnetic diagnostics," Plasma Phys. Controlled Fusion **33**, 715–748 (1991).
[45]B. Faugeras and H. Heumann, "FEM-BEM coupling methods for tokamak plasma axisymmetric free-boundary equilibrium computations in unbounded domains," J. Comput. Phys. **343**, 201–216 (2017).
[46]V. D. Shafranov and L. E. Zakharov, "Use of the virtual-casing principle in calculating the containing magnetic field in toroidal plasma systems," Nucl. Fusion **12**, 599–601 (1972).
[47]S. Mochalskyy, M. Hoelzl, and R. Hatzky, "Parallelization of JOREK-STARWALL for non-linear MHD simulations including resistive walls (report of the EUROfusion high level support team projects JORSTAR/JORSTAR2)," arXiv:1609.07441 (2018).
[48]S. J. P. Pamela, A. Bhole, G. T. A. Huijsmans, B. Nkonga, M. Hoelzl, I. Krebs, and E. Strumberger, "Extended full-MHD simulation of non-linear instabilities in tokamak plasmas," Phys. Plasmas **27**, 102510 (2020).

[49]A. Portone, "The stability margin of elongated plasmas," Nucl. Fusion **45**, 926–932 (2005).
[50]R. Fitzpatrick, "Effect of a nonuniform resistive wall on the stability of tokamak plasmas," Phys. Plasmas **1**, 2931–2939 (1994).
[51]F. Villone, Y. Q. Liu, R. Paccagnella, T. Bolzonella, and G. Rubinacci, "Effects of three-dimensional electromagnetic structures on resistive-wall-mode stability of reversed field pinches," Phys. Rev. Lett. **100**, 255005 (2008).
[52]V. Riccardo, P. Noll, and S. Walker, "Forces between plasma, vessel and TF coils during AVDEs at JET," Nucl. Fusion **40**, 1805 (2000).
[53]V. Yanovskiy, N. Isernia, V. D. Pustovitov, and F. Villone, "Sideways forces on asymmetric tokamak walls during plasma disruptions," Nucl. Fusion **62**, 086001 (2022).
[54]N. Schwarz, F. J. Artola, M. Hoelzl, M. Bernert, D. Brida, L. Giannone, M. Maraschek, G. Papp, G. Pautasso, B. Sieglin, I. Zammuto, ASDEX Upgrade Team, and JOREK Team, "Experiments and non-linear MHD simulations of hot vertical displacement events in ASDEX-Upgrade," Plasma Phys. Controlled Fusion **65**, 054003 (2023).
[55]N. Isernia, G. Rubinacci, N. Schwarz, R. Sparago, F. Vannini, S. Ventre, M. Hoelzl, F. Artola, and F. Villone, "Comparison of the approaches to the solution of the outer magneto-static-problem in free-boundary MHD solvers," in 49th EPS Conference on Plasma Physics, Bordeaux, France, 2023.
[56]F. Cipolletta, N. Schwarz, M. Hoelzl, S. Ventre, N. Isernia, G. Rubinacci, A. Soba, and JOREK Team, "Code optimizations in the BSC advanced computing hub: Implementation of matrix compression for the coupling of JOREK to the 3D realistic conducting wall structures," in Proceedings of the 20th European Fusion Theory Conference, Padova, Italy, 2–5 October 2023.
[57]G. Rubinacci, A. Tamburrino, S. Ventre, and F. Villone, "Application of n-fold rotational symmetries to eddy currents integral model in the time domain," IEEE Trans. Magn. **56**, 1–4 (2020).